

Scalable Quantum Memory Nodes Using Nuclear Spins in Silicon Carbide


Shravan Kumar Parthasarathy^{1,2}, Birgit Kallinger¹, Florian Kaiser^{3,4}, Patrick Berwian¹,
Durga B.R. Dasari^{3,4}, Jochen Friedrich¹, and Roland Nagy^{1,2,*}

¹Fraunhofer Institute for Integrated Systems and Device Technology (IISB), Germany

²Group of Applied Quantum Technologies (AQuT), Friedrich-Alexander-Universität Erlangen-Nürnberg (FAU), Germany

³3rd Institute of Physics and Stuttgart Research Center of Photonic Engineering (SCoPE), University of Stuttgart, Stuttgart 70569, Germany

⁴Center for Integrated Quantum Science and Technology (IQST), Germany

 (Received 1 August 2022; revised 14 December 2022; accepted 31 January 2023; published 8 March 2023)

A distributed quantum network would require quantum nodes capable of performing arbitrary quantum information protocols with high fidelity. So far the challenge has been in realizing such quantum nodes with features for scalable quantum computing. We show here that using the solid-state spins in 4H silicon carbide (4H SiC) such a goal could be realized, wherein a controlled generation of highly coherent qubit registers using nuclear spins is possible. Using a controlled isotope concentration and coherent control we perform here atomistic modeling of the central spin system formed by the electron spin of a silicon-vacancy color center (V_{Si}^- center) and the noninteracting nuclear spins. From this we lay out conditions for realizing a scalable nuclear-spin (^{13}C or ^{29}Si) register, wherein independent control of the qubits alongside their mutual controlled operations using the central electron spin associated to the V_{Si}^- center in 4H SiC are achieved. Further, the decoherence and entanglement analysis provided here could be used to evaluate the quantum volume of these nodes. Our results mark a clear route towards realizing scalable quantum memory nodes for applications in distributed quantum computing networks and further for quantum information protocols.

DOI: [10.1103/PhysRevApplied.19.034026](https://doi.org/10.1103/PhysRevApplied.19.034026)

I. INTRODUCTION

The realization of a distributed quantum computing network, in which local quantum memory nodes (QMN) are connected over long distances via optical photons, is an outstanding challenge in the field of applied quantum technologies [1,2]. The key building block for the realization of a quantum computing network is a QMN representing a hybrid quantum system composed of qubits with different functionalities. They include qubits that form an interface with the flying qubits (photons) and another kind that allows for the processing of quantum information carried by the photons [Fig. 1(a)] [3]. Over the last decade, atomistic spin defects in solids have emerged as a potential candidate in realizing such QMN [4–7]. Many components for the realization of a QMN have already been demonstrated in great details for NV and Si- V color centers in diamond. These realizations include long-lived quantum memory qubits realized through the lattice nuclear spins [6,8,9], and spectrally stable optical transitions of the defect electron spin [10–12]. Furthermore, demonstrations

of embedding them into nanophotonic structures [13,14] and a small-scale quantum network [15] has also been achieved. Despite this progress QMNs with scalable memory registers and at the same time displaying high cooperativities in photonic structures has not been shown so far. We address this challenge and report how the silicon-vacancy color centers (V_{Si}^- centers) in 4H SiC, with controlled doping allows for the realization of a scalable QMN [16–19].

The realization of a QMN requires an optically active quantum system and coherently controllable long-lived memory qubits. Therefore, our analysis considers a single V_{Si}^- center as a control and communication qubit surrounded by ^{13}C and ^{29}Si nuclear spins as memory qubits [20–24]. Electron-nuclear spin interaction is modeled by a central spin model wherein, a single V_{Si}^- center couples to surrounding ^{13}C and ^{29}Si nuclear spin qubits through hyperfine interaction, which is described by the following Hamiltonian [25,26]:

$$H = DS_z^2 + \omega_0 S_z + \omega_n I + \vec{S} \mathbf{A} \vec{I}. \quad (1)$$

The first term in Eq. (1) describes the ground-state zero-field splitting (ZFS), the second and third terms describe

*roland.nagy@fau.de

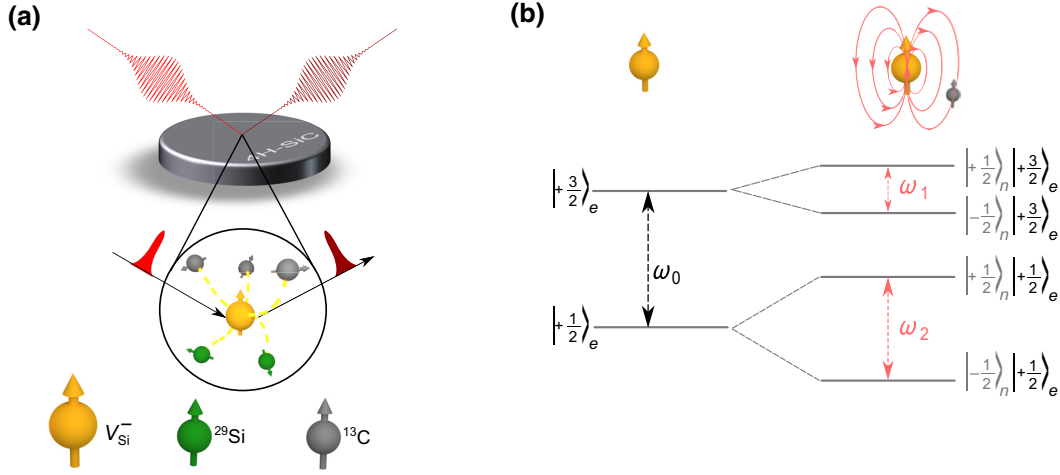


FIG. 1. (a) Schematic representation of a quantum memory node interacting with incoming and outgoing photons. The QMN is made of an electron-nuclear spin system as shown in the illustration. (b) Energy-level scheme for a two-spin subspace ($|3/2\rangle$ and $|1/2\rangle$) of V_{Si}^- center without and with hyperfine coupling to a nuclear spin in the vicinity.

the electron and nuclear Zeeman interaction with an external magnetic field, respectively. Depending on the type of the nuclear spin, the Zeeman interaction differs significantly as the gyromagnetic ratios for the carbon and silicon nuclear isotopes are $\gamma_n = 10.71$ MHz/T (^{13}C), and $\gamma_n = -8.46$ MHz/T (^{29}Si), respectively [26]. The last term describes the hyperfine interaction, where \mathbf{A} is the hyperfine tensor with elements $A_{ij} = (\mu_0 \hbar^2 \gamma_e \gamma_n) (3r_i r_j - \delta_{ij}) / (4\pi r^3)$ [27]. With the magnetic field aligned along the quantization axis of the defect center we can safely neglect the V_{Si}^- center electron spin-flip terms, i.e., the S_x and S_y terms in this hyperfine interaction. With this simplification the hyperfine tensor \mathbf{A} becomes a vector with components $\vec{A} = \{A_{zx}, A_{zy}, A_{zz}\}$. Incorporating this into the nuclear spin Hamiltonian and by projecting it onto the S^z basis of the electron spin, it reduces to

$$H^n = |\pm 3/2\rangle \langle \pm 3/2| \otimes H_{\pm 3/2}^n + |\pm 1/2\rangle \langle \pm 1/2| \otimes H_{\pm 1/2}^n. \quad (2)$$

As noted above the V_{Si}^- -center electron spin is a four-level system (FLS) with eigenbasis states $|\pm 3/2\rangle_e$ and $|\pm 1/2\rangle_e$. The nuclear dynamics conditioned on the electron spin state is determined by $H_{\pm 3/2}^n = \omega_n I_z \pm 3/2(A_{\parallel} I_z + A_{\perp} I_x)$, and $H_{\pm 1/2}^n = \omega_n I_z \pm 1/2(A_{\parallel} I_z + A_{\perp} I_x)$. Instead of working in the full FLS, we restrict the dynamics to the effective $|3/2\rangle_e$ and $|1/2\rangle_e$ two-level subspace. This is realized by an applied static magnetic field with 500 G aligned along the quantization axis of the V_{Si}^- center. The frequency of applied microwave addresses the nuclear spin transitions corresponding to the V_{Si}^- -center electron spin state of $|3/2\rangle_e$ and $|1/2\rangle_e$.

II. CONTROLLABLE NUCLEAR SPIN

A. Pulse sequence to identify a nuclear spin

The realization of a QMN requires coherent control of single nuclear spins via electron-nuclear gate sequences. The main challenge in implementing these sequences is to maintain spin coherence on the electron spin and avoid unwanted crosstalk between nuclear-spin qubits. To address this problem, a control sequence is required, which preserves the spin coherence of the V_{Si}^- center and at the same time also performs a selective rotation on the nuclear-spin qubits. This could be achieved by a pulse sequence, which involves a two-qubit gate based upon phase-controlled rf, which drives the nuclear spins interleaved with dynamical decoupling (DD) of the electron spin [9]. DDrf sequences enable the control of multiple nuclear-spin qubits while maintaining the spin coherence on the electron spin (V_{Si}^- center) and reducing their crosstalk. The concept of DDrf sequences is based on selective two-qubit gates. Therefore, hyperfine interaction is utilized, which couples each nuclear spin to the V_{Si}^- center. This hyperfine interaction depends on the position of the nuclear-spin qubit relative to the V_{Si}^- center [27,28].

We further control the nuclear spins through rf control wherein the applied frequency ω , phase ϕ , and the amplitude (Rabi frequency) Ω are adjusted to allow for independent control and coupling of a given nuclear spin to the V_{Si}^- center electron spin. For example, to address a specific nuclear spin when the V_{Si}^- center is in the spin state $|3/2\rangle_e$, we set $\omega = \omega_1 = \sqrt{(\omega_L - 3A_{\parallel}/2)^2 + 9A_{\perp}^2/4}$ or at $\omega = \omega_2 = \sqrt{(\omega_L - A_{\parallel}/2)^2 + A_{\perp}^2/4}$, when the V_{Si}^- center is in the state $|1/2\rangle_e$. Further, for a very low (negligible) perpendicular coupling A_{\perp} and a Rabi frequency $\Omega \ll (\omega_2 - \omega_1)$, the conditional nuclear Hamiltonian gets

further simplified such that the total Hamiltonian given in Eq. (3) takes the form

$$H^n = |\pm 3/2\rangle\langle\pm 3/2| \otimes \Omega(\cos(\phi))I_x + \sin(\phi)I_y + |\pm 1/2\rangle\langle\pm 1/2| \otimes (\omega_2 - \omega_1)I_z. \quad (3)$$

One can see from the equation above that there is a rotation of the nuclear spin about the x - y plane when V_{Si^-} -center electron spin is conditioned to be in the state $|3/2\rangle_e$ and a phase evolution of nuclear spin about z axis when V_{Si^-} -center electron spin is conditioned to be in the state $|1/2\rangle_e$. The conditional phase evolution is governed by the detuning $(\omega_2 - \omega_1)$ of the applied rf pulse ($\omega = \omega_1$) with the nuclear-spin energy difference (ω_2) when the electron spin is at $|1/2\rangle_e$ [as depicted in Fig. 1(b)], as shown in Eq. (3). A pulse sequence, which utilizes Eq. (3) to identify and coherently control single nuclear-spin qubits via conditional rotations, is shown in [Fig. 2(a)]. The sequence begins by preparing the V_{Si^-} -center electron spin in a superposition state, $1/\sqrt{2}[|1/2\rangle_e + |3/2\rangle_e]$, using a $\pi_y/2$ pulse. After this a controlled rotation CROT(ω) sequence is applied [insert Fig. 2(a)]. When the rf frequency ω is resonant with a given nuclear-spin qubit ($\omega = \omega_1$ or ω_2), the CROT(ω) acts as an electron-nuclear DDrf two-qubit conditional phase rotation as shown in Eq. (3). The phase of each rf pulse on the nuclear spin is labeled as $\phi_{n=1,\dots,N+1}$ with N being the total number of π pulses on V_{Si^-} -center electron spin. Whereas, $N + 1$ denotes the total number of rf pulses on the nuclear spin. If the initial state of the electron spin is $|3/2\rangle_e$ and the rf frequency $\omega = \omega_1$, the nuclear spin will undergo a rotation about x - y plane. The nuclear-spin evolution is followed by a π pulse, which flips the electron spin state from $|3/2\rangle_e$ to $|1/2\rangle_e$. Subsequently the nuclear spin will undergo a free evolution about the z axis. This sequence will be repeated until the $N + 1$ rf pulse on the nuclear spin.

$$\begin{aligned} \phi_1 &= \phi_{\text{initial}}, \\ \phi_2 &= \phi_1 + \phi_{\tau_n} + \pi, \\ \phi_{l+2} &= \phi_l + 2\phi_{\tau_n}, \\ \phi_{N+1} &= \phi_{N-1} + \phi_{\tau_n}. \end{aligned} \quad (4)$$

The phase of each applied nuclear spin rf pulse ($\phi_{n=1,\dots,l,l+1,l+2,\dots,N+1}$) is given by Eq. (4) [9,25]. The phase of the first nuclear-spin rf pulse can be freely set to ϕ_{initial} . Correspondingly, the phase of consecutive rf nuclear-spin pulses is calculated depending on the phase obtained due to the free evolution $\phi_{\tau_n} = (\omega_2 - \omega_1)\tau_n$ for a time period of τ_n as shown in Eq. (4). Furthermore a 180° shift is required between consecutive nuclear-spin rf pulses to alter their rotation direction depending on the electron-spin state [25].

The final readout of the sequence is done by $\pi_\phi/2$ -pulse on the electron spin with varying phase ϕ .

The corresponding results are shown in Fig. 2(b). The reduction in the probability amplitude of the final readout is governed by loss of coherence due to the scenario where $\omega = \omega_1$ or ω_2 . This effect is used for the detection of nuclear spins in the vicinity of a V_{Si^-} center. Using the sequence shown in Fig. 2(a), we perform the numerical simulations to detect the nuclear-spin qubits. For negligible A_\perp (A_{xz} or A_{yz}) coupling, the fidelity of detecting the nuclear spin can be maximized for the number of π pulses $N \gg \pi/(2\Omega\tau_n)$. By varying the driving frequency ω the sequence is capable of detecting randomly positioned ^{13}C and ^{29}Si nuclear-spin qubits. We note that all nuclear-spin qubits show two hyperfine transitions positioned at $\omega = \omega_1$ and $\omega = \omega_2$ (due to the driving of nuclear spins at the corresponding spin state of the V_{Si^-} center). This leads to an additional control, which we discuss later.

B. Nuclear-spin accessibility

Upon turning onto the atomistic modeling of the nuclear-spin bath from the physical parameters associated to the SiC lattice, a volume of 680 nm^3 is considered with the position of the V_{Si^-} center set at the origin for the lattice space. This corresponds to approximately 8200 unit cells of the lattice [25,29]. Further, we consider a natural isotopic abundance of ^{13}C and ^{29}Si nuclear spins to be 1.1% and 4.7%, respectively. With this isotopic concentration, the average distance between any two nuclear spins is larger than 6 nm, indicating a weak (negligible) intranuclear spin interactions. For this reason, in the remainder of the discussion we consider all the nuclear spins of the bath are noninteracting and any interaction between them will be mediated by the V_{Si^-} -center electron spin alone. Further, the average distance at natural isotopic abundance of the V_{Si^-} -center electron spin to the nearest nuclear spins is in the order of 0.5 nm, leading to the coupling strength in the range of Hz to approximately 200 kHz. To optimize the maximum accessible number of controllable nuclear-spin qubits as potential quantum memories we perform a parametric analysis by employing the sequence from Fig. 2(a). A useful property, which influences the outcome of the measurement protocol, is the concentration of nuclear spins that dictates the total number of isotopes in the vicinity of a V_{Si^-} center [30]. To analyze the influence of the isotopic concentration on the maximum number of controllable nuclear spins we initially simulate the measured contrast of a single ^{13}C and ^{29}Si nuclear isotope at all possible positions around a V_{Si^-} center. The contrast in amplitude, as shown in Fig. 2(b), is analyzed using the pulse sequence from Fig. 2(a) for each position (radial r and angular θ coordinates) of a nuclear spin from V_{Si^-} center. The analysis is initially performed for a long nuclear-spin driving time of $\tau_n = 93 \mu\text{s}$ with $N = 100$, which amounts to the total driving time of $2N\tau_n = 18.6 \text{ ms}$ [Fig. 3]. However, the

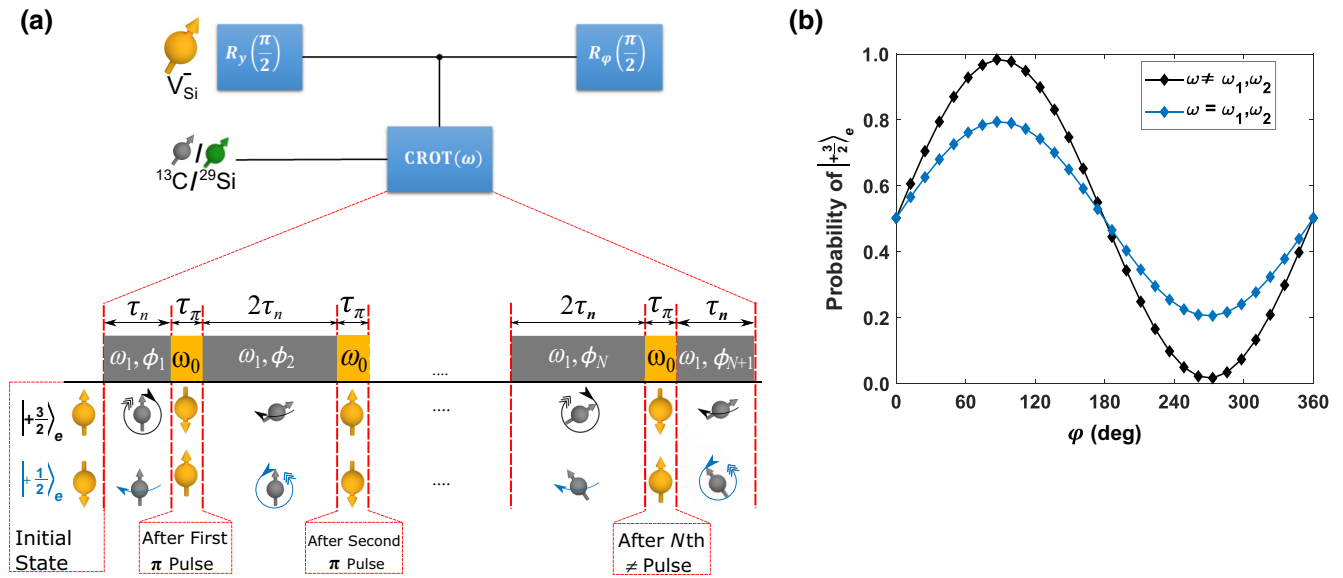


FIG. 2. (a) DDrf pulse sequence used for detecting and controlling nuclear spins with interleaved dynamic decoupling on the V_{Si}^- center to preserve the electron-spin coherence. The sequence also depicts the nuclear spin being driven for a $2\tau_n$ period between electron-spin π pulses. The dynamic decoupling sequence uses N π pulses on the V_{Si}^- -center electron spin. The phase of the n^{th} rf signal, which drives the nuclear spin varies as ϕ_n [9,25]. (b) The result of the final electron-spin state population is readout with varying phase (φ) of our final $\pi/2$ pulse as shown in (a). In the scenario when the rf frequency ω is detuned from the nuclear-spin levels (ω_1 or ω_2), an inversion of spin-state population from $|3/2\rangle_e \Leftrightarrow |1/2\rangle_e$ is observed. Whereas when the rf frequency ω is in resonance with ω_1 or ω_2 [as shown in (a) for $\omega = \omega_1$] a reduction of the probability amplitude between $|3/2\rangle_e \Leftrightarrow |1/2\rangle_e$ is observed.

choice of nuclear-spin driving time is restricted by the V_{Si}^- -center electron-spin coherence. Therefore, this analysis is also performed for a short nuclear-spin driving time $\tau_n = 46$ with μs $N = 20$ (total driving time of $2N\tau_n = 1.8$ ms) [Fig. 4(a)]. However, the simulation shows that the sensing volume within which a nuclear spin can be detected is reduced. This behavior arises due to the fact that the

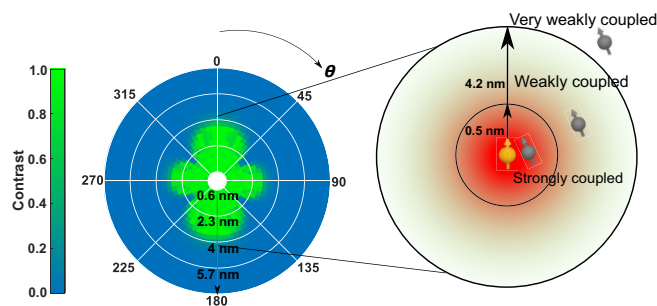


FIG. 3. The contrast in controlling a nuclear spin in the vicinity of a V_{Si}^- -center electron spin is shown as a function of the relative position of nuclear spins in a polar plot. The nuclear spins that are closer to the V_{Si}^- -center electron spin are coupled strongly with a coupling strength $A > (1/T_2^*)$. The nuclear spins that are further away from the central V_{Si}^- -center electron spin require more driving time in order to access them owing to a very low coupling strength. The accessibility of such very weakly coupled nuclear spin are limited by the V_{Si}^- -center electron-spin coherence.

maximum radial distance until which nuclear spins are accessible (for $\theta = 0^\circ$ or $\theta = 180^\circ$) reduces with decreasing nuclear-spin driving time τ_n as depicted in Fig. 4(b). The rise and drops of the contrast in Fig. 4(b) is suspected to be the cause of the revival of the electron-spin coherence when the nuclear spin exhibits a complete rotation. The contrast drop beyond a certain radial distance in Fig. 4(b) indicates that a longer driving time is necessary to access this nuclear spin.

To analyze the usability of nuclear spins we set two criteria. First (i) we consider only nuclear-spin qubits at a

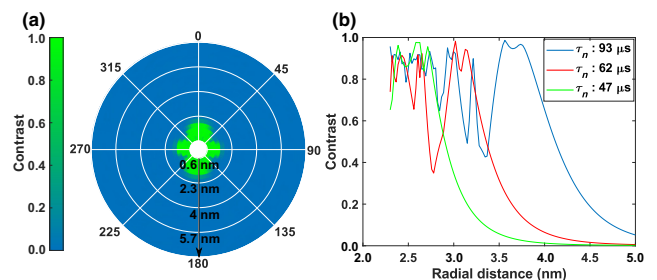


FIG. 4. (a) Polar plot of the nuclear-spin contrast for a fixed values of $N = 20$ and $\tau_n = 46 \mu\text{s}$ is depicted. Nuclear spins closer to the V_{Si}^- -center electron spin (approximately 2 nm) are accessible unlike those shown Fig. 3. (b) The radial dependence on accessing a nuclear spin depending on the contrast for $\theta = 0$ depicts that the radial distance within which the nuclear spins are accessible reduces with decreasing τ_n .

lattice position where the contrast is larger than >0.5 . Second (ii) we consider only nuclear-spin qubits, which can be independently controlled (independent rf driving frequency). Exploiting the interdependence of contrast and rf driving frequency ω we can statistically analyze the controllable nuclear-spin qubits by looking for nuclear spins that satisfy the aforementioned criteria. If we assume a natural abundance of 1.1% of ^{13}C and 4.7% of ^{29}Si , the total number of accessible nuclear spins, which meet the first criteria are $N_{\text{qubits}} = 161$ for $N = 100$ with $\tau_n = 93 \mu\text{s}$ and $N_{\text{qubits}} = 23$ for $N = 20$ with $\tau_n = 46 \mu\text{s}$, respectively. Unfortunately, a high amount of accessible nuclear spins leads to driving of multiple nuclear spins within an identical driving frequency and henceforth to a lower amount of controllable nuclear-spin qubits that could exhibit independent driving [25]. Hence upon following both the criteria at natural abundance of isotopes the $N_{\text{qubits}} = 16$ for $N = 100$

with $\tau_n = 93 \mu\text{s}$ and $N_{\text{qubits}} = 14$ for $N = 20$ with $\tau_n = 46 \mu\text{s}$, respectively.

In our analysis, we are varying the concentration of ^{13}C and ^{29}Si between 0.25% and 5.8%. The variation of isotopic concentration is such that the proportion of ^{13}C is the same as ^{29}Si until ^{13}C concentration reaches its natural abundant concentration (1.1%), beyond which the concentration of ^{29}Si is varied. We are performing a statistical analysis over 1000 distributions for all given concentrations of ^{13}C and ^{29}Si . All nuclear-spin qubits, which do not fulfill both aforementioned criteria are excluded in our analysis.

C. Influence of material and experimental parameters

The total number of accessible nuclear spins at an isotopic concentration of 0.25% (with the sum of

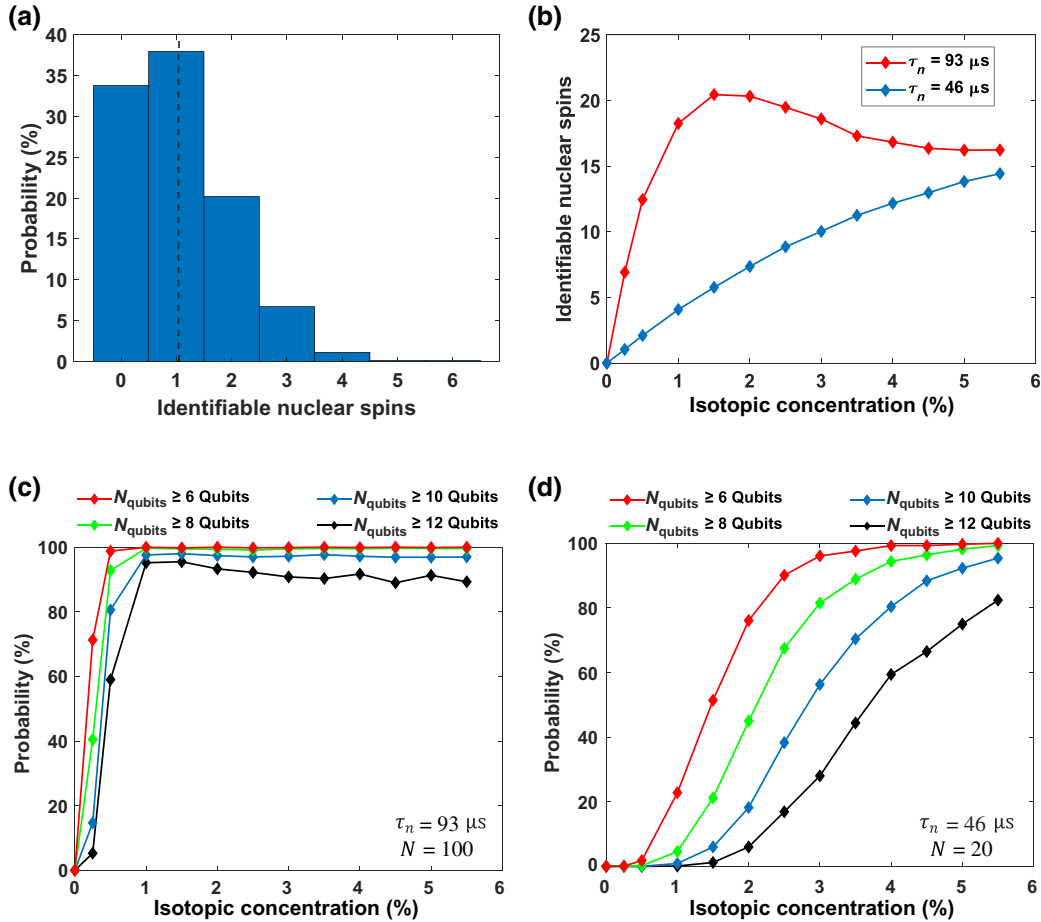


FIG. 5. (a) Histogram on the number of nuclear spins that are independently accessible is plotted for a $[^{13}\text{C}] = 0.125\%$ and $[^{29}\text{Si}] = 0.125\%$ along with the mean accessible nuclear spins (dotted line). The analysis is carried out for 1000 different distribution of nuclear spin around the central V_{Si} -center electron spin. (b) The mean number of accessible nuclear spins for varying isotopic concentrations are depicted for two configurations. The plot reveals a possibility to access 20 nuclear spins at total isotopic concentration of 1.5% for $N = 100$ with $\tau_n = 93 \mu\text{s}$. (c),(d) represents the probability in accessing more as 6 qubits to 12 qubits with varying isotopic concentration for $N = 100$ with $\tau_n = 93 \mu\text{s}$ and $N = 20$ with $\tau_n = 46 \mu\text{s}$, respectively.

$[^{13}\text{C}] = 0.125\%$ and $[^{29}\text{Si}] = 0.125\%$) considering the two aforementioned criteria is shown as a histogram in Fig. 5(a). Wherein the mean accessible nuclear spins and the probability distributions for our analysis are derived. The mean accessible nuclear spins for a sum concentration of ^{13}C and ^{29}Si isotopes are depicted in Fig. 5(b). The curve saturates for $\tau_n = 93 \mu\text{s}$ and $N = 100$ at an isotopic concentration of 1.5%. At the mentioned isotopic concentration there are 49 nuclear-spin qubits within the sensing volume, which meets criterion (i) for $\tau_n = 93 \mu\text{s}$ and $N = 100$. Meanwhile, for $\tau_n = 46 \mu\text{s}$ and $N = 20$ there are only eight nuclear-spin qubits within the sensing volume that meets criterion (i). Owing to more nuclear spins within the sensing volume for $\tau_n = 93 \mu\text{s}$ and $N = 100$ the effect of nonindependent driving within the sensing volume starts to dominate as shown at 1.5% in Fig. 5(b). Hence the mean identifiable nuclear spins for $\tau_n = 93 \mu\text{s}$ with $N = 100$ reduces until the point where the effect of increasing nuclear spins within the sensing volume and deteriorating controllable nuclear spins due to nonindependent driving cancels out. The curve hence saturates at naturally abundant concentration of isotopes [25]. This result shows the relevance of tailored isotopically produced 4H-SiC epitaxial layers to maximize the nuclear-spin qubit access. A similar behavior is also noticeable for $\tau_n = 46 \mu\text{s}$ with $N = 20$, but in this case at a much higher isotopic concentration owing to a smaller sensing volume.

D. Analysis of coherence property

Based on the analysis from Fig. 5(a), it is also clearly indicated in Figs. 5(c) and 5(d) that $N_{\text{qubits}} > 10$ are achievable for both scenarios where $\tau_n = 93 \mu\text{s}$ and $\tau_n = 46 \mu\text{s}$, respectively. The probability distribution can hence be adjusted for one given isotopic concentration by adjusting the nuclear-spin driving time. However, the choice of τ_n and N also depends on the spin-coherence property corresponding to the given isotopic concentration. For further understanding of the relation between spin coherence and isotopic concentration, an investigation is conducted through the method of cluster-correlation expansion (CCE) [25,26,31]. The investigation is realized with static magnetic field of 500 G. The analysis reveals a possibility of preserving the electron-spin coherence up to 2 ms at an isotopic concentration of 1.0%. However the electron-spin coherence deteriorates with increasing isotope concentration. Hence the choice of an optimal rf driving time τ_n for an isotopically pure sample acts as a useful experimental parameter that maximizes the accessible and controllable nuclear-spin qubits per quantum memory node. For instance, a DDrf sequence with $\tau_n = 93 \mu\text{s}$ and $N = 100$ demands the electron-spin coherence time > 18.6 ms while the configuration of $\tau_n = 46 \mu\text{s}$ and $N = 20$ demands the electron-spin coherence time > 1.86 ms.

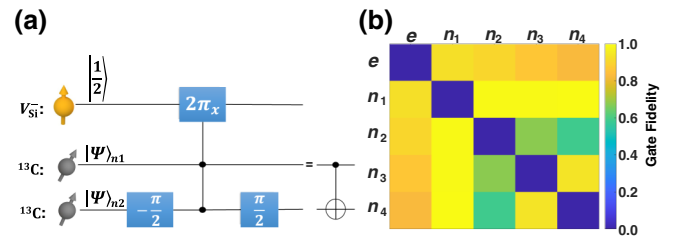


FIG. 6. (a) The V_{Si}^- -center electron-spin-controlled CNOT gate between two uncoupled nuclear spins. The controlled rotation of V_{Si}^- -center electron spin is performed for $|1/2\rangle_{n1}|1/2\rangle_{n2}$ of nuclear spins. (b) For a random choice of nuclear spins at a ^{13}C concentration of 1%, we show the entangling gate fidelities among various nuclear spins. In the above simulation, the couplings of the nuclear spins to the central spin are $\{A_{zz} = 12.5, -3.8, -18.9, 13.4 \text{ kHz and } A_{xz} = 2.3, 5.1, -13, 9 \text{ kHz}\}$, respectively.

III. EXAMINING THE FIDELITY OF CNOT GATE

To determine the efficiency of a quantum computer, alternative indicators, such as quantum volume were introduced recently [32]. These measures determine the actual number of high-fidelity quantum bits that are useful for computing among the many physical qubits available (e.g., 20 on average in our case). To evaluate this measure one needs to perform $\text{SU}(4)$ operations on any two qubits in the quantum register, and this needs the ability to perform a CNOT gate between any two qubits among the detected spins. For this we have performed the analysis on the generation of a CNOT gate between pairs for nuclear spin qubits which potentially plays a pivotal role in generation of a maximally entangled state [9]. The CNOT gate between a V_{Si}^- -center and nuclear spins (n_1, n_2, n_3 and n_4) can be achieved by DDrf sequence through a controlled rotation of a nuclear spin by $\pi/2$ [Fig. 2(a)] [9]. The CNOT gate between a pair of nuclear-spin qubits can only be achieved through the intervention of an electron-spin qubit. The sequence to generate a CNOT gate between a pair of nuclear-spin qubits is shown in Fig. 6(a) [33]. The $\pi/2$ gate operation on nuclear spins are performed through the DDrf sequence as shown in Fig. 2(a). The analysis is conducted at an isotopic spin-bath concentration of 1% with a random spatial nuclear-spin-bath configuration. The result of the simulation as shown in Fig. 6(b) reveals a fidelity $> 90\%$ in the generation of a CNOT gate between two nuclear-spin qubits mediated by a V_{Si}^- -center electron spin.

IV. CONCLUSION AND OUTLOOK

In conclusion, our analysis shows a notable chance of accessing 20 nuclear spin qubits at an isotopic ^{13}C and ^{29}Si concentrations in the range of 1–1.5% [Fig. 5(b)]. Hence a control on isotopic purity is necessary in order to maximize the number of nuclear-spin qubits. A minimum of six memory qubits can be detected with significant probability

of $>20\%$ at an isotopic concentration of 1.0% . A way to increase the register size further is to adjust the experimental driving time τ_n . As shown in Fig. 3(a), longer driving time τ_n increases the sensing volume thereby allowing weakly interacting nuclear-spin qubits to be identified. However, the choice of τ_n is also limited by the electron-spin coherence property, which further limits the sensing volume. Hence, for a low isotopic concentration it would be beneficial to use a long nuclear-spin driving time τ_n and a high number of repetitions N to increase the sensing volume. Unfortunately, electron-spin coherence sets an upper limit for the nuclear-spin driving time and number of repetitions. For a higher isotopic concentration like natural abundance, it would be beneficial to drive the nuclear spins with a shorter nuclear-spin driving time in order to reduce nonindependent driving. Therefore, our presented work gives a detailed answer to the question how many memory qubits can be identified and controlled via a single V_{Si} center. Further with the ability to achieve high-fidelity entangling gates among the nuclear spins and the decoherence analysis performed, one should be able to estimate the quantum volume as a function of the isotopic concentration in these materials.

ACKNOWLEDGMENTS

We acknowledge financial support by the Federal Ministry of Education and Research (BMBF) project QMNDQCNet, and by the Fraunhofer Start Project “Quantum Computing”. DDBRao would like to acknowledge the support by DFG (FOR2724).

-
- [1] A. S. Cacciapuoti, M. Caleffi, F. Tafuri, F. S. Cataliotti, S. Gherardini, and G. Bianchi, Quantum internet: Networking challenges in distributed quantum computing, *IEEE Netw.* **34**, 137 (2020).
- [2] R. Beals, S. Brierley, O. Gray, A. W. Harrow, S. Kutin, N. Linden, D. Shepherd, and M. Stather, Efficient distributed quantum computing, *Proc. R. Soc. A* **469**, 20120686 (2013).
- [3] N. Morioka, C. Babin, R. Nagy, I. Gediz, E. Hesselmeier, Di Liu, M. Joliffe, M. Niethammer, D. Dasari, and V. Vorobyov, *et al.*, Spin-controlled generation of indistinguishable and distinguishable photons from silicon vacancy centres in silicon carbide, *Nat. Commun.* **11**, 2516 (2020).
- [4] A. Bourassa, C. P. Anderson, K. C. Miao, M. Onizhuk, H. Ma, A. L. Crook, H. Abe, J. Ul-Hassan, T. Ohshima, and N. T. Son, *et al.*, Entanglement and control of single nuclear spins in isotopically engineered silicon carbide, *Nat. Mater.* **19**, 1319 (2020).
- [5] R. Nagy, M. Niethammer, M. Widmann, Y.-C. Chen, P. Udvarhelyi, C. Bonato, J. U. Hassan, R. Karhu, I. G. Ivanov, and N. T. Son, *et al.*, High-fidelity spin and optical control of single silicon-vacancy centres in silicon carbide, *Nat. Commun.* **10**, 1954 (2019).
- [6] H. P. Bartling, M. H. Abobeih, B. Pingault, M. J. Degen, S. J. H. Loenen, C. E. Bradley, J. Randall, M. Markham, D. J. Twitchen, and T. H. Taminiau, *et al.*, Coherence and Entanglement of Inherently Long-Lived Spin Pairs in Diamond, *Phys. Rev. X* **12**, 011048 (2022).
- [7] H. Bernien, B. Hensen, W. Pfaff, G. Koolstra, M. S. Blok, L. Robledo, T. H. Taminiau, M. Markham, D. J. Twitchen, and L. Childress, *et al.*, Heralded entanglement between solid-state qubits separated by three metres, *Nature* **497**, 86 (2013).
- [8] S. Yang, Y. Wang, D. D. B. Rao, T. Hien Tran, A. S. Momenzadeh, M. Markham, D. J. Twitchen, P. Wang, W. Yang, and R. Stöhr, *et al.*, High-fidelity transfer and storage of photon states in a single nuclear spin, *Nat. Photonics* **10**, 507 (2016).
- [9] C. E. Bradley, J. Randall, M. H. Abobeih, R. C. Berrevoets, M. J. Degen, M. A. Bakker, M. Markham, D. J. Twitchen, and T. H. Taminiau, A Ten-Qubit Solid-State Spin Register with Quantum Memory up to One Minute, *Phys. Rev. X* **9**, 031045 (2019).
- [10] P. Udvarhelyi, R. Nagy, F. Kaiser, S.-Y. Lee, J. Wrachtrup, and A. Gali, Spectrally Stable Defect Qubits with no Inversion Symmetry for Robust Spin-To-Photon Interface, *Phys. Rev. Appl.* **11**, 044022 (2019).
- [11] R. Nagy, D. B. R. Dasari, C. Babin, Di Liu, V. Vorobyov, M. Niethammer, M. Widmann, T. Linkewitz, R. Stöhr, and H. B. Weber, *et al.*, Narrow inhomogeneous distribution of spin-active emitters in silicon carbide, *Appl. Phys. Lett.* **118**, 144003 (2021).
- [12] L. J. Rogers, K. D. Jahnke, T. Teraji, L. Marseglia, C. Müller, B. Naydenov, H. Schauffert, C. Kranz, J. Isoya, and L. P. McGuinness, *et al.*, Multiple intrinsically identical single-photon emitters in the solid state, *Nat. Commun.* **5**, 4739 (2014).
- [13] C. Babin, R. Stöhr, N. Morioka, T. Linkewitz, T. Steidl, R. Wörnle, Di Liu, E. Hesselmeier, V. Vorobyov, and A. Denisenko, *et al.*, Fabrication and nanophotonic waveguide integration of silicon carbide colour centres with preserved spin-optical coherence, *Nat. Mater.* **21**, 67 (2022).
- [14] A. Sipahigil, R. E. Evans, D. D. Sukachev, M. J. Burek, J. Borregaard, M. K. Bhaskar, C. T. Nguyen, J. L. Pacheco, H. A. Atikian, and C. Meuwly, *et al.*, An integrated diamond nanophotonics platform for quantum-optical networks, *Science (New York, N.Y.)* **354**, 847 (2016).
- [15] M. Pompili, S. L. N. Hermans, S. Baier, H. K. C. Beukers, P. C. Humphreys, R. N. Schouten, R. F. L. Vermeulen, M. J. Tiggelman, L. Dos Santos Martins, and B. Dirkse, *et al.*, Realization of a multinode quantum network of remote solid-state qubits, *Science (New York, N.Y.)* **372**, 259 (2021).
- [16] R. Nagy, Silicon vacancy defects in 4H-silicon carbide semiconductor for quantum applications (2019), <https://doi.org/10.18419/opus-10653>.
- [17] D. J. Christle, A. L. Falk, P. Andrich, P. V. Klimov, J. U. Hassan, N. T. Son, E. Jánzén, T. Ohshima, and D. D. Awschalom, Isolated electron spins in silicon carbide with millisecond coherence times, *Nat. Mater.* **14**, 160 (2015).
- [18] M. Niethammer, M. Widmann, T. Rendler, N. Morioka, Y.-C. Chen, R. Stöhr, J. U. Hassan, S. Onoda, T. Ohshima, and S.-Y. Lee, *et al.*, Coherent electrical readout of defect

- spins in silicon carbide by photo-ionization at ambient conditions, *Nat. Commun.* **10**, 5569 (2019).
- [19] M. Widmann, S.-Y. Lee, T. Rendler, N. T. Son, H. Fedder, S. Paik, L.-P. Yang, N. Zhao, S. Yang, and I. Booker, *et al.*, Coherent control of single spins in silicon carbide at room temperature, *Nat. Mater.* **14**, 164 (2015).
- [20] D. J. Christle, P. V. Klimov, C. F. de las Casas, K. Szász, V. Ivády, V. Jokubavicius, J. Ul Hassan, M. Syväjärvi, W. F. Koehl, and T. Ohshima, *et al.*, Isolated Spin Qubits in SiC with a High-Fidelity Infrared Spin-to-Photon Interface, *Phys. Rev. X* **7**, 021046 (2017).
- [21] Y.-C. Chen, P. S. Salter, M. Niethammer, M. Widmann, F. Kaiser, R. Nagy, N. Morioka, C. Babin, J. Erlekampf, and P. Berwian, *et al.*, Laser writing of scalable single color centers in silicon carbide, *Nano Lett.* **19**, 2377 (2019).
- [22] F. Fuchs, B. Stender, M. Trupke, D. Simin, J. Pflaum, V. Dyakonov, and G. V. Astakhov, Engineering near-infrared single-photon emitters with optically active spins in ultrapure silicon carbide, *Nat. Commun.* **6**, 7578 (2015).
- [23] D. Riedel, F. Fuchs, H. Kraus, S. Váth, A. Sperlich, V. Dyakonov, A. A. Soltamova, P. G. Baranov, V. A. Ilyin, and G. V. Astakhov, Resonant Addressing and Manipulation of Silicon Vacancy Qubits in Silicon Carbide, *Phys. Rev. Lett.* **109**, 226402 (2012).
- [24] R. Nagy, M. Widmann, M. Niethammer, D. B. R. Dasari, I. Gerhardt, Ö.O. Soykal, M. Radulaski, T. Ohshima, J. Vučković, and N. T. Son, *et al.*, Quantum Properties of Dichroic Silicon Vacancies in Silicon Carbide, *Phys. Rev. Appl.* **9**, 034022 (2018).
- [25] See Supplemental Material at <http://link.aps.org/supplemental/10.1103/PhysRevApplied.19.034026> for an explanation regarding spin Hamiltonian, DDrf pulse sequence, and spin-coherence property.
- [26] L.-P. Yang, C. Burk, M. Widmann, S.-Y. Lee, J. Wrachtrup, and N. Zhao, Electron spin decoherence in silicon carbide nuclear spin bath, *Phys. Rev. B* **90**, 241203 (2014).
- [27] K. R. K. Rao and D. Suter, Characterization of hyperfine interaction between an NV electron spin and a first-shell ^{13}C nuclear spin in diamond, *Phys. Rev. B* **94**, 060101 (2016).
- [28] B. Smeltzer, L. Childress, and A. Gali, ^{13}C hyperfine interactions in the nitrogen-vacancy centre in diamond, *New J. Phys.* **13**, 25021 (2011).
- [29] Takuma Kobayashi, Kou Harada, Yu Kumagai, Fumiyasu Oba, and Yu-Ichiro Matsushita, Native point defects and carbon clusters in 4H-SiC: A hybrid functional study, *J. Appl. Phys.* **125**, 125701 (2019).
- [30] H. Seo, A. L. Falk, P. V. Klimov, K. C. Miao, G. Galli, and D. D. Awschalom, Quantum decoherence dynamics of divacancy spins in silicon carbide, *Nat. Commun.* **7**, 12935 (2016).
- [31] W.-L. Ma, G. Wolfowicz, N. Zhao, S.-S. Li, J. J. L. Morton, and R.-B. Liu, Uncovering many-body correlations in nanoscale nuclear spin baths by central spin decoherence, *Nat. Commun.* **5**, 4822 (2014).
- [32] A. W. Cross, L. S. Bishop, S. Sheldon, P. D. Nation, and J. M. Gambetta, Validating quantum computers using randomized model circuits, *Phys. Rev. A* **100**, 032328 (2019).
- [33] G. Waldherr, Y. Wang, S. Zaiser, M. Jamali, T. Schulte-Herbrüggen, H. Abe, T. Ohshima, J. Isoya, J. F. Du, and P. Neumann, *et al.*, Quantum error correction in a solid-state hybrid spin register, *Nature* **506**, 204 (2014).